DOI: 10.13009/EUCASS2022-6191
9TH EUROPEAN CONFERENCE FOR AERONAUTICS AND SPACE SCIENCES (EUCASS)

Study of the effect of the presence of particles on the plume of rocket engines

*Angelica Maria Toscano**
** University of Salento, Department of Engineering for Innovation*
angelica.tosc@hotmail.it
*Maria Grazia De Giorgi***
*** University of Salento, Department of Engineering for Innovation*
mariagrazia.degiorgi@unisalento.it

Abstract

The thermal radiation signature produced by rocket engine exhaust plumes is a challenging phenomenon to analyze. The thermal emissions are affected by several characteristics, such as motor type; propellant type, liquid or solid; additives in each propellant; burn time; rocket geometry and results are influenced by other causes such as the trajectory of the rocket, the atmosphere conditions, the models used for the calculation of gas and particles radiative properties. A detailed description of radiative particle's properties, as well as the measurement of the exhaust plume temperature and its distribution, are important, because radiative heat transfer leads to a rise of the rocket surface temperature by several hundred degrees, resulting in a deterioration of the rocket base. Moreover, the rocket plume plays an important role in the operation of target detection, tracking, classification, and identification. The rocket thermal radiation is in visible, infrared, and ultraviolet regions. The infrared radiation mostly is given by the gas radiation of some combustion products as CO_2 and H_2O, and the continuous spectral radiation of smoke solid microparticles. In the solid rocket motor propellant generally, there are additives such as boron and aluminum. The Al_2O_3 particles in the exhaust plume produce emission spectra in the ultraviolet band due to the high temperature that reaches values in the range 2000-3000K. The unburned fuels in the exhaust plume generate high concentrations of C, N, and H, among which the chemical reactions produce a large number of free photons that contribute to ultraviolet radiation. In this paper, a signature analysis procedure was developed to understand the spectral characteristics of exhaust plumes in detail and the effect of alumina concentration on the emitted radiation. To study the exhaust plume leaving the nozzle outlet, the compressible flow through and beyond the rocket engine nozzle was predicted by a CFD code. The turbulent flow of the high-speed combustion jet was described with the axisymmetric form of the Navier Stokes equation coupled with the turbulence model k - ω, solved with a pressure-based solver formulation with second-order weighted upwind central spatial discretization. Substantial efforts have been directed to studying the effects of afterburning reactions and alumina concentrations on IR signatures and on the Schlieren visualization and predicting how different parameters of the propellant components affect the spectral radiation signature of the exhaust plume.

1. Introduction

The IR signature of an aerospace vehicle arises from multiple sources such as hot parts and skin emissions, reflected sunshine, skyshine, and earthshine emissions, and engine exhaust plume radiation. Proper optimization and an accurate study of radiative properties are necessary because radiative heat transfer increases the surface temperatures of rocket and spacecraft components by several hundred degrees causing premature corrosion of components. The aim of this work is the analysis of infrared signature spectral characteristics from the motor exhaust plumes. The infrared irradiance signature of the plume depends on several characteristics such as motor type, propellant ingredients, motor operating parameters, and flight conditions. In recent decades, solid fuel combustion propulsion of aircraft and spacecraft has become the most popular choice for rocket propulsion systems. The reasons for this success are a wide range of applications, lower production costs, simplicity, and safety. In a typical solid rocket motor (SRM) the propellant grain is stored and burned in the same tank after the combustion products pass through a convergent-divergent (De Laval) nozzle where with a rapid expansion the exhaust jet is formed. The exhaust gases of rockets leave the nozzle outlet at very high temperatures, and knowledge of thermal emissions produced, particularly those at infrared (IR) wavelengths is a crucial aspect during the design and the tests of the rocket motors. Generally, in the solid propellant composition, there are additives such as boron and aluminum. These additives increase thrust level, at the same time the aluminum reacts with combustion products as CO_2, H_2O, and O_2 and produces alumina

DOI: 10.13009/EUCASS2022-6191

Al_2O_3 . Alumina is accumulated on the burning particles' surface and is the first source of intense thermal infrared emission in the plume. Therefore, substantial effort has been directed to the study of the alumina in the plume for the accurate prediction of radiative heating. The Al_2O_3 particles in the exhaust plume produce emission spectra in the ultraviolet band due to the high temperature that reaches values in the range 2000-3000K. Moreover, the high-temperature iron oxide particles also emit in the ultraviolet spectrum. In the past several effort has been done to the study of the alumina optical properties, i.e. absorption index and the refractive index, for the accurate prediction of radiative heating.Finally, the unburned fuels in the exhaust plume generate high concentrations of C, N, and H, among which the chemical reactions produce a large number of free photons, and the chemiluminescence participated by these free photons will also produce ultraviolet radiation [1]. Prediction of the radiative heat transfer from a rocket engine exhaust plume is a very complex problem, involving rocket geometry, propellant composition, combustion modeling, fluid mechanics, atmosphere modeling, calculation of gas and particles' radiative properties, and radiative transfer through the atmosphere. Consequently, the development of simplified models with fast and flexible solution methods is required. In the literature, some efforts have been made to reveal the radiative properties of particles and the radiative heat transfer process inside the SRM by considering the thermal radiation of particles [2, 3]. However few studies analyzed the effect of particle concentration on both radiation and density gradient field, which could be captured by optical techniques. To experimentally visualize the simulated high-speed flow in the cases discussed above, the suitable optical techniques are the Schlieren and Shadowgraph. These techniques permit to visualization complex flow phenomena, representing visualizations of the first and second derivatives of the flow field refractive index, directly related to density. This work aims to predict how the presence of alumina particles affects the signature of the spectral radiation and well as the Schlieren acquired flow field of the exhaust plume and to verify that it is possible to study the particle concentration and distribution through the development of non-intrusive techniques.

2. CFD modeling of the rocket plume

The Eulerian-Lagrangian method is used for the simulation of the two-phase flow field. The radiative properties of alumina particles are obtained from Mie theory. The radiative properties of local particles are input into the radiative transfer equation to estimate the radiation intensity and the heat source term by radiation in the energy equation.

2.1 Two-phase flow modeling

The model includes the turbulence and species transport equations, and is defined as:

$$\frac{\partial U}{\partial t}+\frac{\partial E}{\partial x}+\frac{\partial F}{\partial r}+\frac{H}{r}=\frac{\partial Ev}{\partial x}+\frac{\partial Fv}{\partial xr}+\frac{Hv}{r}+S \tag{1}$$

where U is the conservative variable vector, E , F and H are the convective flux vectors; E*v*, F*v* and H*v* are the viscid flux vectors; S is the sources term. x and r are the axial and radial coordinates and t is the time term. Considering the exhaust plume as a hot, turbulent, reactive, and radiating flow, at low altitude, the terms chemical source S*c* and radiative source S*r* can be introduced as vectors within the term S.
The trajectory of alumina particle in the flowfield is found by integrating the force balance on the particle. In the force balance equation, the particle inertia equates to the forces acting on the particle.

$$\frac{dy}{dx}=F_D\left(\overrightarrow{u_g}-\overrightarrow{u_p}\right)+\frac{\vec{g}\,(\rho_p-\rho_g)}{\rho_p}+\vec{F} \tag{2}$$

The last two terms are both set as zero i.e. the force of gravity and additional acceleration. The first term is the drag force per unit particle mass and in Ref.[4] is defined as:

$$F_D=\frac{18\mu_g}{\rho_p d_p^2}\frac{C_D\,Re}{24} \tag{3}$$

The drag coefficient C_D for smooth particles is given by:

DOI: 10.13009/EUCASS2022-6191

$$C_D = a_1 + \frac{a_2}{Re} + \frac{a_3}{Re^2} \tag{4}$$

Where constants a_1, a_2, and a_3 are given by Morsi and Alexander [5].
For the heat transfer of particles, the convection between particles and gas, and the radiative heat transfer among particles and the surfaces are considered.

2.2 Chemistry Modeling in AfterBurning

The main chemical species emitted by solid rocket motor are CO, H_2, H, N_2, H_2O, CO_2, Cl, and HCl. The afterburning process in an SRM jet consists of the oxidation of hydrogen molecules and carbon monoxide emitted by the SRM, forming O, OH, H, water H_2O, and carbon dioxide CO_2. A system of reactions based on finite-rate chemistry is used to predict the post-combustion effect [6], defined as:

$$\sum_{j=1}^{N_r} v'_{ij}\, W_i \leftrightarrows \sum_{j=1}^{N_r} v''_{ij}\, W_i \qquad (i = 1,2, \dots \dots \dots, \mathrm{N_r}) \tag{5}$$

v'_{ij}, v''_{ij} = stoichiometric coefficients for the reactant and the i-th product in the j-th reaction
N_r = number of chemical species in this reaction system
k_{fi}, k_{fj} = Rate constants of the forward reaction and backward reaction.
The latter are determined by Arrhenius relation:

$$k_f = AT^n e^{\left(-\frac{E_a}{RT}\right)} \tag{6}$$

A= pre-exponential factor
n = the temperature exponent
E_a= activation energy
The i_{th} species $\dot{\omega}_i$ is given as:

$$\dot{\omega}_\mathrm{i} = \left(v'_{ij} - v''_{ij}\right)\left[k_{fi}\prod_{j=1}^{N_r}\left(\frac{\rho_{ij}}{W_i}\right)^{v'_{ij}} - k_{bj}\prod_{j=1}^{N_r}\left(\frac{\rho_{ij}}{W_i}\right)^{v''_{ij}}\right]W_i \tag{7}$$

ρ_{ij} is the density of the i_{th} reactant or product in the j_{th} reaction. During hydrogen combustion, free radical products are involved in the partial conversion of the HCl, present in the exhaust gas, in Cl e Cl_2. Wang et al. [7] showed about 90% of HCl molecules are unreacted at an altitude 0,5 km, so they can also be neglected. Other chemical processes occur between the ambient gases and the hot gases expelled from the combustion chamber. These include NO_x and OH formation, which may have an impact on local ozone loss. As reference was made to the system N_2 / O_2 given by Oliveira and Patel [8], 13 primary chemical species were considered; as O_2, N_2, H_2, CO, CO_2, H_2O, HO_2, HCl, N, NO, OH, H and O. A chemical model described by a mechanism of 28 reactions was used, with detailed data of the chemical reactions [6] for afterburning, listed in the Table3.

Table 3: Chemical reactions for the prediction of afterburning in the exhaust plume. Units in cm, mol, cal, s.

[a] H_2O = 6.0; [b] H_2 = 2.0, H_2O = 6.0; [c] H_2O = 5.0; [d] H_2 = 2.0, H_2O = 16.0; [e] H_2O = 15.0; [f] CO_2 = 3.8, CO = 1.9, H_2 = 2.5, H_2O = 12.0.

N°	*Reactions*	*A*	*n*	*E_a*	*Reference*
1	$H_2 + O_2 \leftrightarrow HO_2 + H$	1.00e+14	0.00	5.60e+04	[9]
2	$H + O_2 \leftrightarrow OH + O$	2.60e+14	0.00	1.68e+04	[9]
3	$O + H_2 \leftrightarrow OH + H$	1.80e+10	1.00	8.90e+03	[9]
4	$OH + H_2 \leftrightarrow H_2O + H$	2.20e+13	0.00	5.15e+03	[9]
5	$2HO \leftrightarrow H_2O + O$	6.30e+12	0.00	1.09e+03	[9]
6[a]	$H + OH + M \leftrightarrow H_2O + M$	2.20e+22	-2.00	0.00e+00	[9]
7[b]	$2H + M \leftrightarrow H_2 + M$	6.40e+17	-1.00	0.00e+00	[9]
8[c]	$H + O + M \leftrightarrow OH + M$	6.00e+16	-0.60	0.00e+00	[9]

DOI: 10.13009/EUCASS2022-6191

9[d]	$H + O_2 + M \leftrightarrow HO_2 + M$	2.10e+15	0.00	-1.00e+03	[9]
10	$HO_2 + H \leftrightarrow 2HO$	1.40e+14	0.00	1.08e+03	[9]
11	$HO_2 + H \leftrightarrow H_2O + O$	1.00e+13	0.00	1.08e+03	[9]
12	$HO_2 + O \leftrightarrow O_2 + OH$	1.50e+13	0.00	9.50e+02	[9]
13	$HO_2 + OH \leftrightarrow H_2O + O_2$	8.00e+12	0.00	0.00e+00	[9]
14	$2HO_2 \leftrightarrow H_2O_2 + O_2$	2.00e+12	0.00	0.00e+00	[9]
15	$H + H_2O_2 \leftrightarrow H_2 + HO_2$	1.40e+12	0.00	3.60e+03	[9]
16	$O + H_2O_2 \leftrightarrow OH + HO_2$	1.40e+13	0.00	6.40e+03	[9]
17	$OH + H_2O_2 \leftrightarrow H_2O + HO_2$	6.10e+12	0.00	1.43e+03	[9]
18[e]	$H_2O_2 + M \leftrightarrow 2HO + M$	1.20e+17	0.00	4.55e+04	[9]
19	$2O + M \leftrightarrow O_2 + M$	6.00e+13	0.00	-1.80e+03	[9]
20	$CO + OH \leftrightarrow CO_2 + H$	1.50e+7	01.30	-7.65e+02	[10]
21	$CO + O_2 \leftrightarrow CO_2 + H$	2.53e+12	0.00	4.77e+04	[10]
22[f]	$CO + O + M \leftrightarrow CO_2 + M$	2.51e+13	0.00	-4.54e+03	[10]
23	$HCl + H \leftrightarrow H_2 + Cl$	2.30e+13	0.00	3.50e+03	[10]
24	$Cl_2 + H \leftrightarrow HCl + Cl$	8.59e+13	0.00	1.17e+03	[10]
25	$HCl_2 + OH \leftrightarrow H_2O + Cl$	2.45e+12	0.00	1.10e+03	[10]
26	$HCl_2 + O \leftrightarrow OH + Cl$	5.24e+12	0.00	6.40e+03	[10]
27	$Cl + Cl + MO \leftrightarrow Cl_2 + M$	2.34e+14	0.00	-1.80e+03	[10]
28	$H + Cl + MO \leftrightarrow HCl + M$	7.20e+21	-2.00	0.00e+03	[10]

A, n and E_a are reaction rate variables. M is a third body expressed as $\sum \frac{\rho_i}{W_i} k_{c,i}$, where ρ_i is the density of the *i*th reactant; $k_{c,i}$ is the third body coefficient of species *i*.

2.3 Radiation Transfer Modeling

The RTE equation must be solved along different in each point of the flow field and each calculation phase, requiring a very expensive procedure. However, Saladin and Farmer [11] stated that the radiative source within the gaseous radiation is negligible compared to other terms, as the solution showed no appreciable difference in the temperature field. Furthermore, the radiation/convection coupled model on a solid rocket engine plume of a single gas species reported by Wang [4] and Kim [12] has an infrared radiation intensity similar to the solution of the decoupling model. Each radiation model has advantages and disadvantages, in this study the DO model was used. This model is based on the resolution of the radiation transfer equation (RTE), taking into account the effects of emission, scattering, and reflection. There are two implementations: uncoupled and (energy) coupled. The decoupled implementation uses a conservative finite volume approach, where the equations for energy and radiation intensities are solved one by one. While in the coupled case, the discrete equations of energy and intensity in each cell are solved simultaneously, assuming that the spatial neighbors are known. The advantage of using the latter lies in accelerating applications involving high optical thicknesses and or high diffusion coefficients. The radiation transfer equation determines the local spectral intensity of the radiation and, in the case of a multi-species hot exhaust plume, is expressed as [6]:

$$\frac{dI_\lambda(s,\mathbf{s})}{ds} = k_\lambda(s) I_{\lambda b}(s) - k_\lambda(s) I_{\lambda b}(s,\mathbf{s}) - \sigma_{s\lambda} I_\lambda(s,\mathbf{s}) + \frac{\sigma_{s\lambda}(s)}{4\pi} \int_{4\pi} I_\lambda(s,\mathbf{s_i})\, \Phi_\lambda(s,\mathbf{s_i}) d\Omega_i \quad \textbf{(8)}$$

where λ indicates the wavelength, I_λ is the local spectral intensity, k_λ and $\sigma_{s\lambda}$ are the absorption and scattering coefficients, respectively. $I_{\lambda b}$ is the Planck blackbody function, and Φ_λ is the spectral scattering phase function. s and **s** represent position and direction that can be integrated over 4π solid angle $d\Omega_i$.

2.4 Alumina particles' radiation properties

The main radiative properties are given by the spectral scattering efficiency $Q_{sca,k}$, the spectral absorption efficiency $Q_{abs,k}$ and spectral scattering phase function U_k.
For an individual alumina particle, the spectral radiative properties can be estimated by Mie theory [13].
The radiative properties depend on the particle diameter D, temperature T and complex index of refraction m = n+ik.
The following relationships are usually used for the estimation of the absorption index k and the refractive index n:

DOI: 10.13009/EUCASS2022-6191

Bakhir et al. [14]

$$k = 0.002(0.06\lambda^2 + 0.7\lambda + 1)\exp\left(1.847(T^* - 2.95)\right) \quad (9)$$

$$T^* = {}^{T}/_{1000} \quad (10)$$

Kuzmin et al. [15]

$$\log k = -2.19 + 0.089\lambda^{0.95} - 0.00056(3200 - T)\lambda^{-0.45} \quad (11)$$

$$n = 1.747 + 0.0066\lambda - 0.0068\lambda^2 + 0.00003 \times T \quad (12)$$

Dombrovsky [16]

$$n = \left[1 + \lambda^2\left(\frac{1.024}{\lambda^2 - 0.00376} + \frac{1.058}{\lambda^2 - 0.01225} + \frac{5.28}{\lambda^2 - 321.4}\right)\right]^{0.5} \quad (13)$$

$$T^* = {}^{T}/_{1000} \times [1 + 0.0202(T^* - 0.473)] \quad (14)$$

In the previous formulas, T is the temperature in K and λ the wavelength. In the present work k has been estimated using the Bakir [14] equation and n using the Kuzmin et al. [15].

Figure 1a reports the scattering coefficient μs, absorption efficiency q_{ab} and scattering efficiency q_{ab} factors calculated by the Mie theory at T = 2900 K and alumina particle diameter D = 1.0 μm. In the short wavelength regime, the efficiency factors are high and fluctuate while they are stable in the long-wavelength regime. The scattering efficiency factor is high in the short wavelength regime, in comparison to the absorption factor, because of the effect of diffraction. Even though the radiative properties of particles are a function of their complex refractive index, the scattering coefficient is mainly influenced by the refractive index and weakly by absorption index while absorption of the particle is influenced by the absorption index and weakly influenced by refractive index.

The alumina particles emit nearly as a gray body in the plume of a solid rocket motor with aluminized propellants. Hence the gray body approximation could be adopted in this study and the effective gray radiative properties could be used and could be estimated from the integration with respect to wavelength. Figure 1b report the total absorption efficiency Q_{ab} and scattering efficiency Q_{sc} factors for particle diameter equal to 1.0 μm.

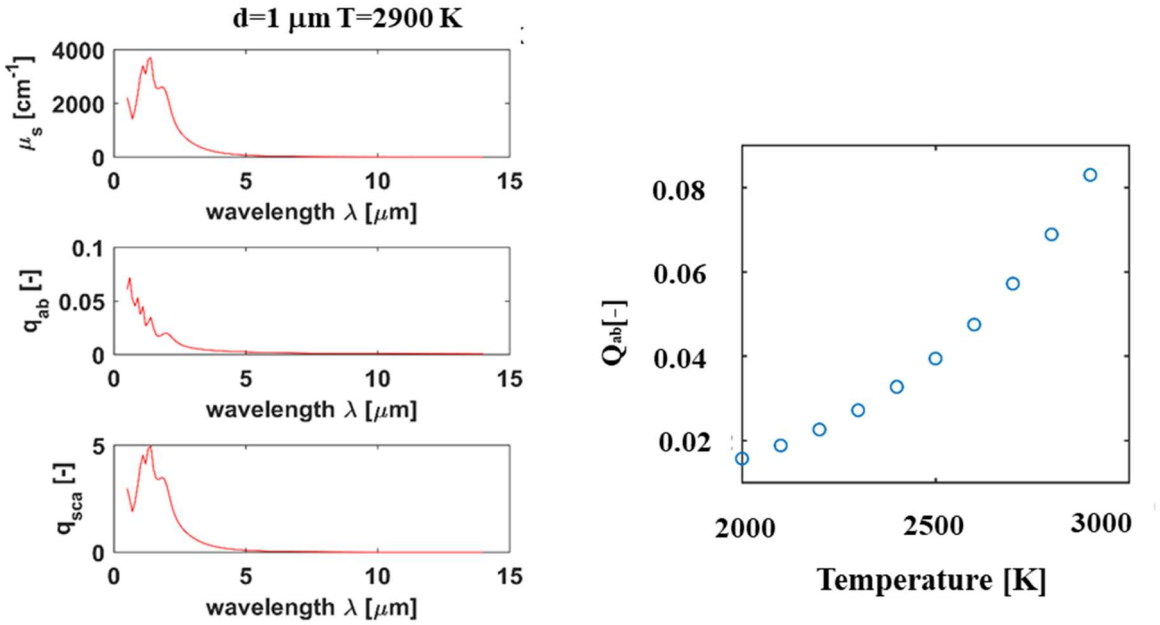

a) b)

Figure 1: a) Scattering Coeffient μs, absorption efficiency q_{ab} and scattering efficiency q_{sc} factors at T = 2900 K and D = 1.0 μm in the function of the wavelength b) Total absorption efficiency Q_{ab} for particle diameter equal to 1.0 μm

2.5 Test case and computational domain

To validate the numerical methodologies, numerical results will be compared with experimental results of the study [17] where the exhaust plume of the small Ballistic Evaluation Motor type-II (BEM-2) motor for Israel Military Industries Ltd.(IMI) [6] was tested in a test-bed facility. In the study, IR images of the plume were obtained with an

DOI: 10.13009/EUCASS2022-6191

IR camera equipped with narrow bandpass filters, and spectroradiometric measurements of the plume were performed.

The rocket exhaust jet is formed by a rapid expansion of high temperature and high-pressure combustion products at supersonic speeds at the exit of a converging-diverging nozzle. Describing its behavior is a complex task, so Computational Fluid Dynamic simulation techniques represent a useful tool for obtaining experimental measurements. For the plume infrared radiation simulation, the CFD code ANSYS Fluent 2021 is used in this paper to deal with the flow field of the compressible gas of the plume. Despite the purpose of this study is to analyze the performance of the aluminate propellant, the first simulations were performed considering that the propellant ingredients did not include metal additives so that the numerical results on IR spectra of the rocket plume could be compared with the experimental results. . Due to the spatial axial symmetry of the plume flow field, the domain has been simplified into a symmetric two-dimensional (2-D) wedge, which will greatly save the computing sources and time (see figure 2). The axial two-dimensional domain of 0.6 m × 2.5 m has been shown in figure 1. The throat diameter of the nozzle was 15 mm, the exit diameter was 22.5 mm and the divergence angle was 15° [6]. The origin of coordinates was set to be in the nozzle inlet center. Partial magnification of the mesh in a specific area is given to demonstrate the emphasis on crucial areas, i.e., nozzle throat and boundaries, where flow parameters change rapidly.

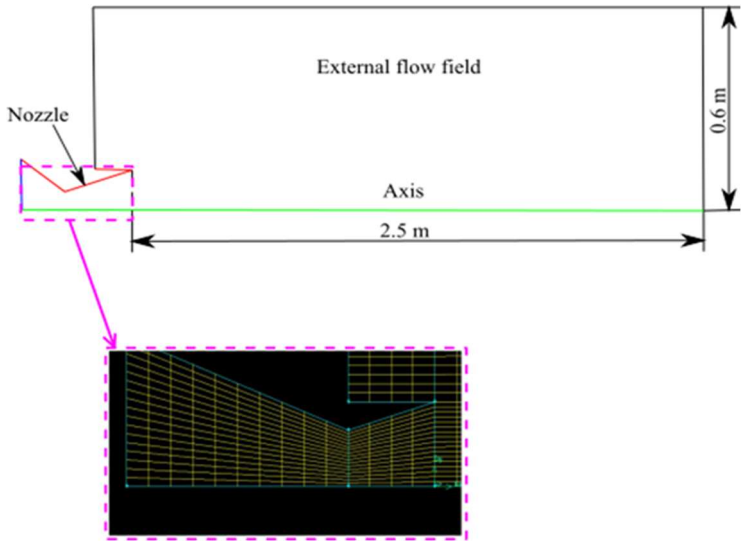

Figure 2: Computanional domain and grid

A pressure-based coupled solver formulation with weighted second-order central-upwind spatial discretizations is applied to calculate the numerical solutions of the time-dependent Navier-Stokes equations.
The hybrid initialization method is used to calculate the gas-phase fluid field and then the result is used as the initialized fluid field for the two-phase flow calculation. The compressible flow inside an aluminized solid rocket motor can be considered as consisting of a continuous phase and a discrete particle phase, given by the alumina particles [18]. The Reynolds averaged Navier – Stokes equations with the turbulence model k–ω is adopted to predict the airflow field, while the Eulerian-Lagrangian method was adopted for the solution of the two-phase flow field. Navier-Stokes equations are solved in the fluid considered a continuum while the discrete phase is solved by tracking the particles. There is an exchange of momentum, mass, and energy between the continuum and discrete phases which was taken into account in the simulations with alumina particles.
Different cases were simulated with various percentages of alumina added with respect to the total mass flow. The cases analyzed are reported in Table 1.
A Rosin-Rammler Diameter Distribution has been used with the mean diameter of aluminum-oxide particles equal to $6.1e^{-6}$ m, temperature 2930 K and axial velocity 150 m/s. By including the radiation source term in the energy balance equation, the plume field calculation and the radiative transfer calculation were carried out in a coupled way. The DO radiation method was used to solve the radiative transfer equation. Alumina emissivity was set equal to 0.2 [2] Setting DO model leads to setting the spectral bands, listed in tab. 2, in which the software must calculate the infrared radiation signature. To study the infrared radiation signature in the seven spectral bands, the flow field and

radiation transfer were calculated in every spectral band. Therefore the distribution of the radiative illumination in the set bands was obtained.

Table 1: Analytical model investigations: test matrix and operating conditions.

Test Case	Percentages of Al_20_3
sim 1	Purely gaseous exhaust flow
sim 2	Flow with 1% of alumina particles
sim 3	Flow with 2.5% of alumina particles
sim 4	Flow with 5% of alumina particles

Table 2: Spectral band division.

Spectral Band	Start [μm]	End [μm]
Band 0	10	6.25
Band 1	6.25	5.1282
Band 2	5.1282	4.6512
Band 3	4.6512	4.1667
Band 4	4.1667	3.2258
Band 5	3.2258	2.6316
Band 6	2.6316	2.2223

For the radiation of multi-component gas, it is usually assumed that the emission coefficient of each gas component is decoupled, the gas absorption coefficient can be calculated using the WSGG model [19]
The boundary conditions are set as follows: the bottom of the simulation domain is the axis, the outlet and inlet of the free flow field is set as static pressure equal to 101325 Pa, and the inlet boundary condition of the nozzle is total pressure equal to 3328000 Pa. The other boundaries are set as free flow. The temperature of the gas at the nozzle inlet is set as 2930 K. The initial ratio of the gas composition is reported in Table 3.

Table 3: Initial species fraction for at the nozzle inlet

Species Mass Fraction	
CO	0.13
CO_2	0.12
H_2	0.07
H_2O	0.4

The gas density has been calculated using the ideal gas model. The density of alumina has been assumed equal to 2800 kg/m^3 and the specific heat capacity is 1525 J/(kg·K).
The effective gray scattering coefficient and absorption coefficient of alumina particles have been calculated as explained in section 2.4.

3. Virtual Flow Visualization Techniques

3.1 Virtual Infrared Images for Exhaust Plume

A unique capability of infrared camera systems is the ability to capture highly detailed video or still images of areas or events that are not immediately visible to the naked eye. Ideally, IR cameras are used where the emissivity values are large. For example, infrared images of the solid rocket engine exhaust plume can reveal features such as plume structure, turbulent flow, and shock diamonds. It was necessary to include IR cameras when studying the thermal emissions of the plume.
To predict the infrared image for a specific camera, and compare it with experiments, it is important to calculate the irradiance of all the pixels.

DOI: 10.13009/EUCASS2022-6191

A camera consists of a matrix of pixels in its focal plane (Field Of View) and each pixel in turn receives radiation from its IFOV (Instantaneous Field of View). There is a relationship between the pixel and the target that allows for defining the incident irradiance on the IFOV. It is possible to define the angular projection of the sensor in the IR image of a single-pixel as [20]:

$$\Omega_{IFOV} = (a \times b)/f^2 = (a' \times b')/R^2 \tag{15}$$

where $(a \times b)$ is the pixel size, f is the focal length, R is the distance between the optical system and the target, and $(a' \times b')$ is the pixel area projected on the object plane. Each pixel receives a radiant flux defined by the following expression [20]:

$$\Phi = \mathrm{L}A\Omega\tau_0\tau_{r(R)} \tag{16}$$

L represents the radiance of the pixel's projected area in the target plane. A is the projected area. τ_0 and $\tau_{(R)}$ are the transmittance of the optical system and atmospheric respectively. Ω is the solid angle of front optics which is determined from distance R and the front optics diameter D_0 [20]:

$$\Omega = (\pi\, \mathrm{D}_0)/(4f^2) \tag{17}$$

Therefore, the incident irradiance is defined as [20]:

$$E = \frac{\Phi}{(a \times b)} = \left(\frac{L\pi\ \ {}_0^2\tau_0\tau_{(R))}}{4f^2}\right) \tag{18}$$

The model can predict the infrared image of different imaging systems by changing the parameters, such as IFOV and space resolution.

3.2 Shadowgraph and Schlieren Techniques

Other techniques considered in this paper for plume visualization are the optical techniques of Schlieren and Shadowgraph. The Schlieren and Shadowgraph techniques are based on the variation of the refractive index in a transparent medium. The fundamental principle is that light rays traveling in a vacuum, or space, travel uniformly in a straight line unless some obstacle alters their direction, in this case, the light rays refract and deviate from their continuous path. Therefore, the density gradients alter the path of light rays and these deviated rays rearrange the light energy distribution on a screen for the shadowgraph system, or interact with a knife-edge in a schlieren system to produce brightness or luminance changes at an image plane. The relation between the density of a fluid and its refractive index n is given by Gladstone–Dale law [21]:

$$n - 1 = k\rho \tag{19}$$

where k is a constant for a given fluid. However, the images obtained in a schlieren technique do not directly show n, but rather its gradients $\frac{\partial n}{\partial x}$ and $\frac{\partial n}{\partial y}$. In shadowgrams it is the 2nd spatial derivative (Laplacian) that is displayed. Considering a right-handed x, y, z coordinate system, we take the z axis as the normal direction; that is, the direction of optical propagation of undisturbed rays which approach the inhomogeneity zone. Optical inhomogeneities have been shown to refract or bend light rays in proportion to their refractive index gradients in an x, y plane, and the resulting ray's curvature is given by [18]:

$$\frac{\partial^2 x}{\partial^2 z} = \frac{1}{n}\frac{\partial n}{\partial x}, \quad \frac{\partial^2 y}{\partial^2 z} = \frac{1}{n}\frac{\partial n}{\partial y} \tag{20}$$

By integrating these components in the x and y directions, we get [18]:

DOI: 10.13009/EUCASS2022-6191

$$\varepsilon_x = \frac{1}{n}\int \frac{\partial n}{\partial x}\partial z, \quad \varepsilon_y = \frac{1}{n}\int \frac{\partial n}{\partial y}\partial z \tag{21}$$

For 2D Schlieren, this become [18]:

$$\varepsilon_x = \frac{L}{n_0}\frac{\partial n}{\partial x}, \quad \varepsilon_y = \frac{L}{n_0}\frac{\partial n}{\partial y} \tag{22}$$

with L which is the length along the optical axis and n_0 is the refractive index of the surrounding medium. It's understandable how gradients $\frac{\partial n}{\partial x}$ and $\frac{\partial n}{\partial y}$ are the cause of refraction. From these equations, it follows that the rays are always deflected towards the region in which n_0 is highest or, in the case of gases, in the direction of a positive density gradient. In a Schlieren image, the illuminance level responds to the first spatial derivative of the refractive index $\frac{\partial n}{\partial x}$, while the shadowgraphy responds to the second spatial derivative or Laplacian $\frac{\partial^2 n}{\partial^2 x}$.

4. Results

4.1 Grid independence analysis

The following section describes the procedure to verify that the cells grid number is sufficient to obtain convergent results In the grid convergence study the meshes analyzed are respectively made with: 246199, 345170 and 490712 cells. The Grid Convergence Index (GCI) proposed by Roache [22] and based on generalized Richardson extrapolation was calculated to measure the percentage of error committed when simulations are run with a coarser grid. The GCI in terms is given by 16.

$$\mathrm{GCI} = \frac{f_{s\,|\in|}}{r_N^P - 1} \tag{23}$$

r_N is the grid refinement ratio and f_s is the safety factor. The safety factor is set to 1.25, because three grids were used for the study. r_N is equal to 2 as recommended by Roache. P is the order of accuracy of the algorithm, evaluated with the Eq.

$$P = \ln\frac{f_3 - f_2}{f_2 - f_1}/\ln(r_N) \tag{24}$$

Finally, the relative error $|\in| = (f_1 - f_2/f_1)$ in which f_1 and f_2 are the values of the static temperature obtained for the fine and medium grids, respectively. GCI_{12} is obtained, namely the grid convergence index from medium to fine grids, while GCI_{23} is that from coarse to medium grids. Ensuring $\frac{GCI_{23}}{r_N^P GCI_{12}} \approx 1$, it is verified that the grids are in the asymptotic interval of convergence. A compromise was found between accuracy and computation time for the grid, then a uniform grid of 345170 cells was employed for simulations.

4.2 Comparison of experimental and numerical results

To validate the numerical procedure used in this study to obtain plume incident radiation, a comparison study was carried out between the case without alumina particles and the experimental results taken from the studies by Avital and Devir [17, 1]. Figures 3 and 4 show the comparison between the experimental measurements of Mach number and the radiation and the predictions obtained with the numerical procedure.

DOI: 10.13009/EUCASS2022-6191

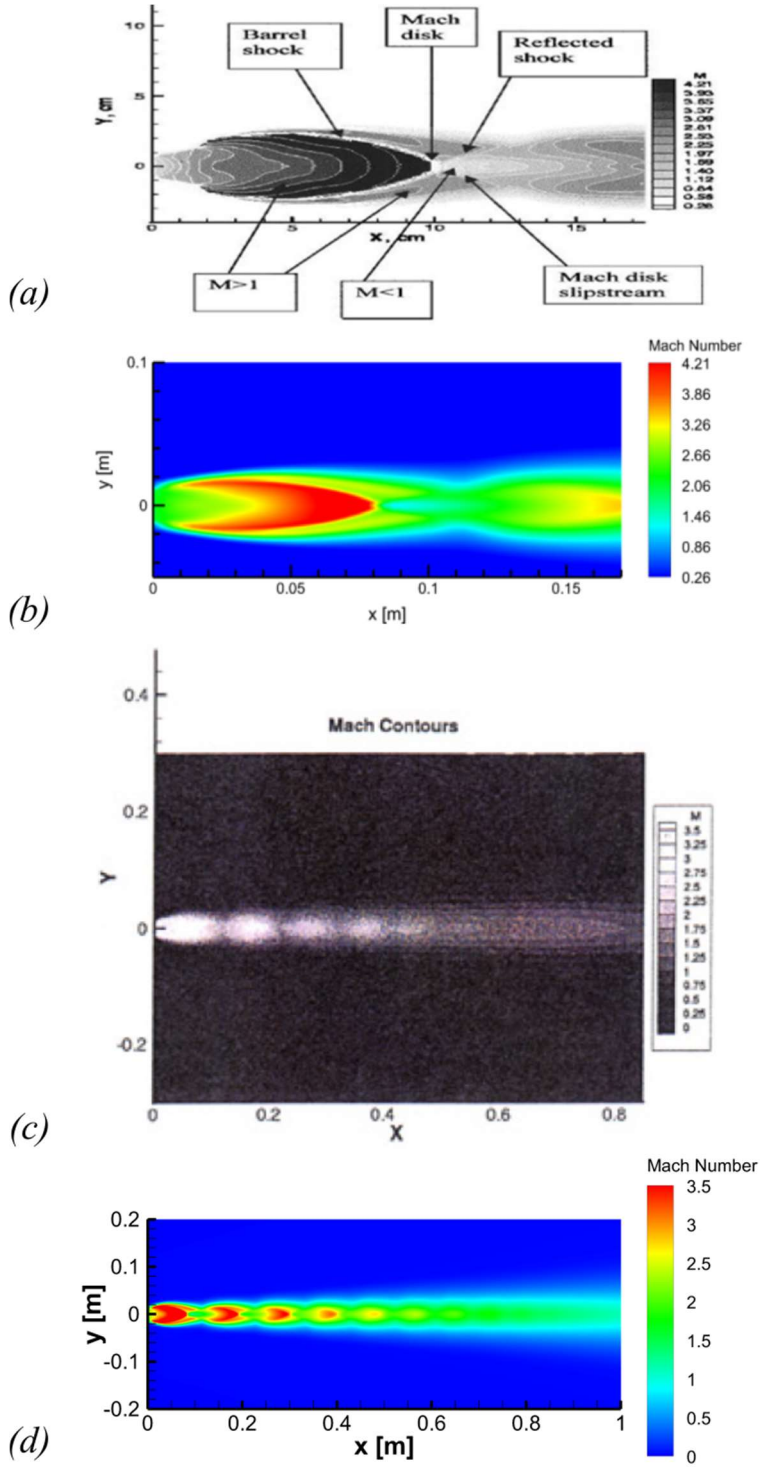

Figure 3: Comparison between the detail of the “Mach disk” in the contour image calculated with CFD (a), and the detail of the “Mach disk” in the experimental image obtained with spectroradiometric measurements for the BEM-2 plume (b) ref. [17] , comparison between the contour of the Mach number calculated with CFD (c), and the experimental image obtained with spectroradiometric measurements for the BEM-2 plume (d) ref. [1].

In figure 3, the experimental image focuses attention on the plume behavior in the near field zone where the characteristic structure of the plume for the under-expanded nozzle are evident.

The result demonstrates that the number of “Mach disk” and the corresponding positions captured by the numerical simulation are in good agreement with the measurements.

As pointed out in the figure, the plume cross-section begins bigger when the distance from the nozzle outlet section increases and the flow accelerates. In this zone, the Mach number is greater than 1 and there is an expansion of the flow due to the Prandtl-Meyer expansion fans. These are reflected on the axis of the nozzle and end up on the walls of the jet generating compression waves. The coalescence of the compression waves produces a barrel shock, where

DOI: 10.13009/EUCASS2022-6191

the maximum value of Mach is found, M = 4.2. The barrel shock collapses to a “Mach disk”, a normal shock wave. The intersection between the “Mach disk” and the barrel shock, originates another reflected shock. Hereafter, the whole pattern repeats, showing several diamonds. Downstream, mixing the plume with ambient air causes the diamonds to fade. The structure described above is visible both in the image obtained experimentally in the laboratory and in that obtained with numerical simulations.

Figure 4 shows the comparison between the predicted radiative intensity and the experimental radiation of BEM-2 [6], using a spectroradiometer. The infrared emission of the numerical case, on the other hand, was obtained with the numerical calculation model aforementioned. To obtain the desired radiance measurement, the incident radiation must be multiplied by the solid angle Ω of front optics which was determined in the formula [Eq. 17]. In this case the object plane $(a \times b)$ is 1.53 m^2 instead R the distance between the target and the lens is 9.4 m [17]. So the solid angle results $\Omega = 1.73 \cdot 10^{-2}$. The comparison of the intensity radiation images between calculations and experiments has been made in the band range 4.6512 - 4.1667 μm. The experimental spectra represent the intrinsic radiation of the plume measured by spectroradiometer calibration to the removal of the atmospheric absorption, hence atmospheric absorption is not considered in calculations. The IR contour shows “diamond” distributions and irradiance intensities in good agreement with the experiments. A good agreement is evident both in terms of intensity and the number of disks.

In the near field, the IR irradiance intensity changed significantly in presence of alumina particles compared with the pure gas. Radiative intensity increases with the amount of alumina concentration, as shown in figure 5, this is because alumina is the first source of intense thermal infrared emission in the plume. This is more evident in figure 6 which shows the axial profile of the incident radiation for the different alumina concentrations. In the near field at the exit of the nozzle, the case of 15% of particle concentration presents the incident radiation value that is double the one of the pure gas phase.

To visualize the effect of particles on the density gradient visualization techniques, virtual Schlieren images were obtained for the CFD simulations, as shown in Figures 7 and 8. In these cases, the gradient has been applied to the gas phase density field, which does not produce real synthetic Schlieren images but approximates them with dignity.

Increasing the concentration of the alumina particles the shock wave structure in the near field area of the plume was obviously changed, in particular, the intensity of Mach disks decreased with respect to the pure gas phase. The results indicated that the existence of particles causes velocity lag.

Hence in presence of alumina there were less distinct diamonds whose distance intervals reduced, and the position of the first diamond moved backwards.

Schlieren images the gradient of the Discrete Particles concentration field was also obtained (see Figure 8). The results of the realistic images of Schlieren exploit the principle of refraction to allow the visualization of the differences in density of the transparent media, therefore the figures show the increase of the dark zone with the increase of alumina particles and allow us to state that it is possible to estimate qualitatively the effect of particle concentration also by visible imaging.

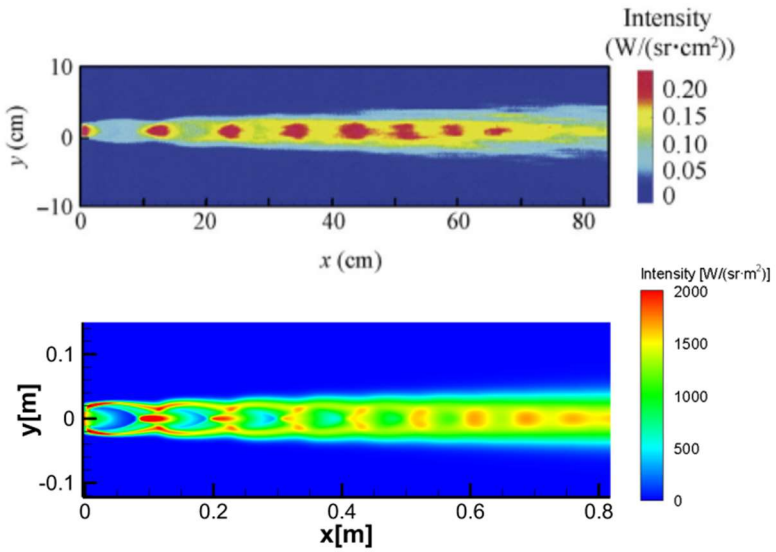

Figure 4: Comparison between the contour of radiative intensity calculated with the numerical procedure and experimental image obtained with spectroradiometric measurements for the BEM-2 plume.

DOI: 10.13009/EUCASS2022-6191

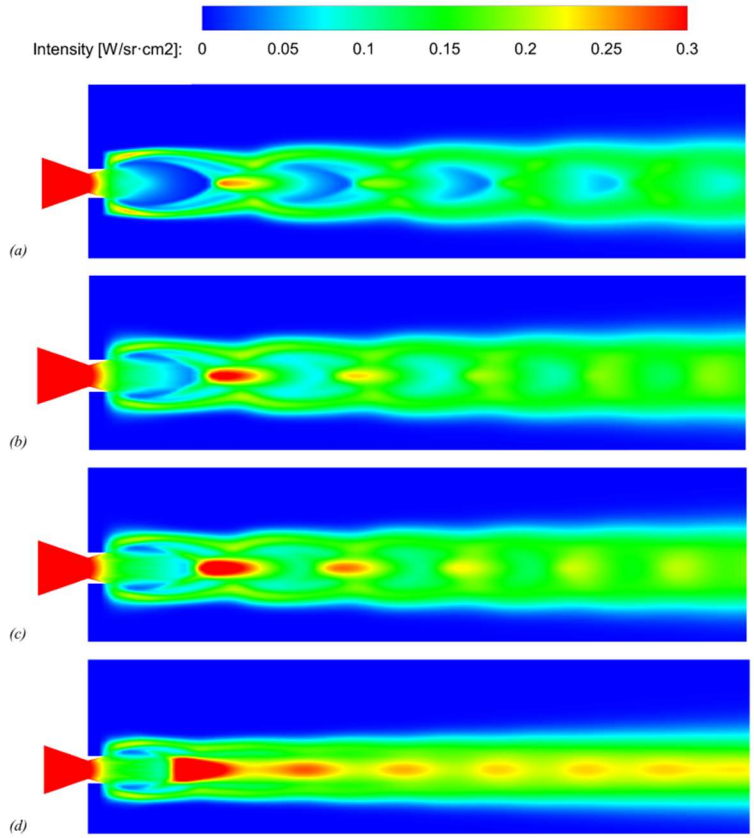

Figure 5: Contour plot of the Radiative Intensity (I) of BEM-2 plume as a function of the percentages of the alumina (Al_3O_2): (a) 0%; (b) 5%; (c) 10%; (d) 15%.

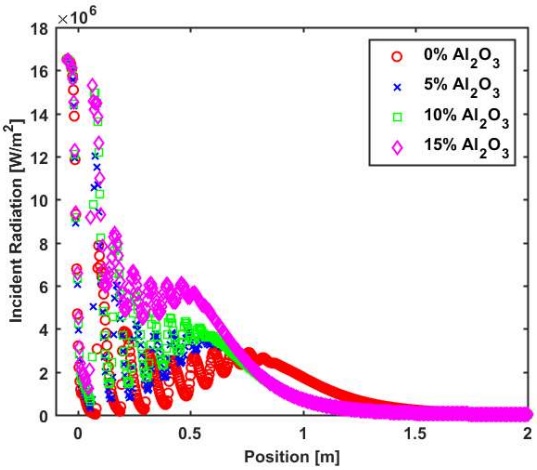

Figure 6: Comparison between the predicted incident radiation at different alumina concentrations

DOI: 10.13009/EUCASS2022-6191

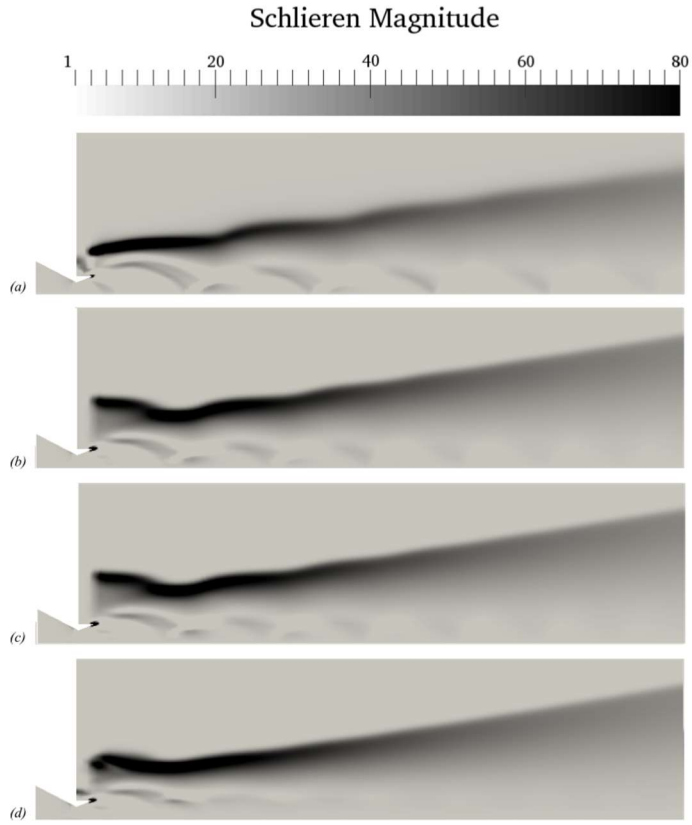

Figure 7: Virtual Schlieren Images at different alumina concentration values: a) pure gas-phase condition, b) Flow with 5% of alumina particle; c) Flow with 10% of alumina particle; d) Flow with 15% of alumina particles.

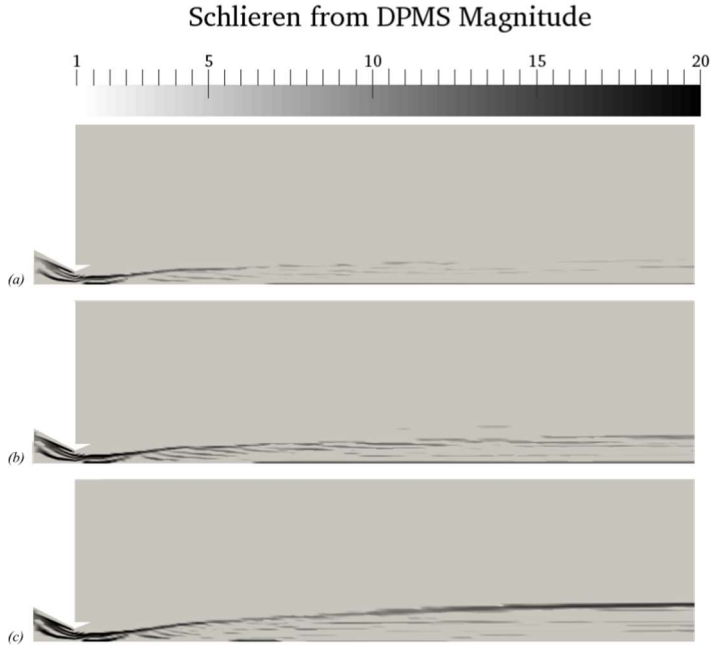

Figure 8: Schlieren Magnitude based on DPM concentrations for cases with radiative interaction. a) Flow with 5% of alumina particle; b) Flow with 10% of alumina particle; c) Flow with 15% of alumina particles.

DOI: 10.13009/EUCASS2022-6191

5. Conclusions

The study analyzes how the presence of alumina affects the properties of the plume of a solid-propellant rocket. In particular, the study analyzes how the alumina agglomerates present in the plume influence the radiative properties. The numerical analysis of the plume flow and infrared radiation characteristics of the solid engine is carried out by two-phase simulations and chemical reactions for the analysis of the afterburning. The following conclusions are obtained: Al_2O_3 solid particles have a significant effect on the flow field of the plume that can be acquired by Schlieren imaging. In presence of alumina there were less distinct diamonds whose distance intervals reduced, and the position of the first diamond moved backwards. The particles interact strongly with the gas and modify the shock wave structures and the radiation spectrum. In the short-wavelength band, the solid particle radiation has a significant impact. Al_2O_3 can affect the radiation contribution by increasing up to 50% of the value of the incident radiation in the band range 4.6512 - 4.1667 μm at the nozzle exit.

Funding

This project received funding from the PON GENERAZIONE E (Cod. ARS01_011318) PNR 2015-2020.

References

[1] Devir, A., Lessin, A., Cohen, Y., Yavin, S., Kanelbaum, Avital, G., Gamss, L., Macales, J., Trieman, B., Lev, M. 2001. Comparison of calculated and measured radiation from a rocket motor plume. In: 39th Aerospace Sciences Meeting and Exhibit, p. 358.
[2] Ko, JY., Lee, E., Kwon, S. 2019. Influence of optical properties of alumina particles on the radiative base heating from solid rocket plume. Adv Space Res ;64(2):514–26.
[3] Harrison, J., Brewster, MQ. 2009. Simple model of thermal emission from burning aluminum in solid propellants. J Thermophys Heat Transf ;23(3):630–4.
[4] Wilcox, D. 2006. Turbulence modeling for cfd. 3rd edn. la canada, california: Dcw industries.
[5] S. Morsi, Alexander, 1972, Investigation of Particle Trajectories in 2.
[6] Qinglin, N., Zhihong, H., Shikui, D. 2017. Ir radiation characteristics of rocket exhaust plumes under varying motor operating conditions. Chinese Journal of Aeronautics. 30 (3) 1101–1114.
[7] Wang, W.-c., Wei, Z.-j., Zhang, Q., Tang, J.-n., Wang, N. 2010. Study on infrared signature of solid rocket motor afterburning exhaust plume. 46th AIAA/ASME/SAE/ASEE Joint Propulsion Conference & Exhibit.
[8] Vu, B., Oliveira, J., Patel, D. 2011. Combustion model of supersonic rocket exhausts in an entrained flow enclosure. In: 20th AIAA Computational Fluid Dynamics Conference, p. 3210.
[9] Gerlinger, P., Moebius, H., Brueggmann, D. 2001. An Implicit Multigrid Method for Turbulent Combustion .In: Journal of Computational Physics pp. 247–276.i:1.10.1006/jcph.2000.667 do
[10] Troyes, J., Dubois, I., Borie, V., Boischot, A. 2006. Multi-Phase Reactive Numerical Simulations of a Model Solid Rocket Exhaust Jet. In: 42nd AIAA/ASME/SAE/ASEE Joint Propulsion Conference&Exhibit. American Institute of Aeronautics and Astronautics. 10.2514/6.2006-4414
[11] Farmer, R., Saladino, A. 1993. Radiation/convection coupling in rocket motors and plumes. In:NASA CONFERENCE PUBLICATION, NASA, pp. 991–991.
[12] Kim, M. T., Song, S., Yim, Y. J., Jang, M. W., Baek, G. 2015. Comparative study on infrared irradiance emitted from standard and real rocket motor plumes, Propellants, Explosives, Pyrotechnics. 40 (5) 779–785.
[13] M.F. Modest Radiative heat transfer (3rd ed.), Academic Press, New York (2013), pp. 387-408.
[14] L.P. Bakhir, G.I. Levashenko, V.V. Tamanovich Refinement of the imaginary part of the complex refractive index of liquid aluminum oxide J. Appl. Spectrosc., 26 (3) (1977), pp. 378-383.
[15] V.A. Kuzmin, E.I. Maratkanova, I.A. Zagray, R.V. Rukavishnikova Thermal radiation of heterogeneous combustion products in the model rocket engine plume Thermophys. Aeromech., 22 (3) (2015), pp. 371-386.
[16] L.A. Dombrovsky Radiation Heat Transfer in Disperse Systems Begell House, New York (1996).

[17] Avital, G., Cohen, Y., Gamss, L., Kanelbaum, Y., Macales, J., B. Trieman, Yaniv, S., Lev, M., Stricker, J., Sternlieb, A. 2001. Experimental and computational study of infrared emission from underexpanded rocket exhaust plumes. Journal of thermophysics and heat transfer 15 (4) 377–383.
[18] Jung, J. –Y., Brewster, M. Q. 2008. Radiative heat transfer analysis with molten al2o3 dispersion in solid rocket motors. Journal of Spacecraft and Rockets. 45 (5) 1021–1030.
[19] Yu, M. J., Baek, S. W., Park, J. H. 2000. An extension of the weighted sum of gray gases non-gray gas radiation model to a two phase mixture of non-gray gas with particles. International Journal of Heat and Mass Transfer 43(10), 1699-1713.
[20] Mei, F., Chen, S., Jiang, Y., Cai, J. 2011. A preliminary model of infrared image generation for exhaust plume, International Journal of Image, Graphics and Signal Processing 3 (4) 46.
[21] Settles, G. S., Covert, E. 2002. Schlieren and shadowgraph techniques: Visualizing phenomena in transport media, Appl. Mech. Rev. 55 (4) B76–B77.
[22] Roache, P.J. 1998. Verification and Validation in Computational Science and Engineering, Hermosa Publishers, Albuquerque, New Mexico.